Available online at www.sciencedirect.com
SCIENCE DIRECT
Acta Materialia 54 (2006) 2027–2039
Acta MATERIALIA
www.actamat-journals.com

Three-dimensional analysis of particle coarsening in high volume fraction solid–liquid mixtures

D.J. Rowenhorst [a], J.P. Kuang [a], K. Thornton [b], P.W. Voorhees [a,*]

[a] Department of Materials Science and Engineering, Northwestern University, Evanston, IL 60208, USA
[b] Department of Materials Science and Engineering, University of Michigan, Ann Arbor, MI 48109, USA

Received 8 September 2005; received in revised form 5 December 2005; accepted 6 December 2005
Available online 15 March 2006

Abstract

The three-dimensional microstructure of 78 and 52 vol.% Sn-rich particles coarsened within a liquid Pb–Sn matrix were determined by the reconstruction of serial sections. The three-dimensional particle size distribution (PSD) and the particle–particle contact distributions were determined. The three-dimensional PSDs do not match those predicted by particle coarsening theory, but there is reasonable agreement with the grain size distributions predicted by a grain growth simulation. In addition, when the particle–particle contact distribution is normalized to the average number of particle contacts, the distribution is statistically invariant with volume fraction. At 52 vol.% it is found that the number of contacts is proportional to the square of the average particle size, but this is not true for 78 vol.%. This is attributed to the increased shape distortions of the particles that are present in the higher volume fraction samples.

Keywords: Coarsening; Grain growth; Image analysis

1. Introduction

Ostwald ripening occurs in multi-phase materials and is a diffusional process in which a system lowers its total energy by reducing the total interfacial area. In a two-phase system, large particles grow at the expense of smaller particles. As the system coarsens, the average particle size increases, while the total volume fraction of particles remains constant. Thus, there is a reduction in the average particle density within the system. Ostwald ripening occurs in many two-phase mixtures and can have a major effect on the properties of a material. For example, coarsening in precipitation-hardened alloys has a significant effect on materials properties, since the decrease in particle density leads to a degradation of the mechanical strength of the alloy.

Initial investigations into the kinetics of Ostwald ripening of particles within a matrix were performed by Greenwood [1], where the growth rates of individual particles within a dispersion of particles were determined theoretically, assuming that the particles are infinitely separated from each other. The results compared qualitatively well to experimental results, but the theoretical treatment did not address the evolution of the size distribution of particles.

The original description of the kinetics of Ostwald ripening of a distribution of particles was proposed by Lifshitz and Slyozov [2] and Wagner [3]. They examined the coarsening of infinitely separated, spherical particles. In the limit where $t \to \infty$, a similarity solution was found, wherein the microstructure should become self-similar when scaled by the average particle size and the average particle size increased with time as $t^{1/3}$.

While this theory captured some more important underlying physics of the coarsening process, it suffered from an unrealistic assumption of a zero volume fraction of the coarsening phase. Much of the later theoretical work has examined the effects of interparticle diffusional interactions that occur in systems with a finite volume fraction [4–13].

* Corresponding author. Fax: +1 847 491 7820.
E-mail address: p-voorhees@northwestern.edu (P.W. Voorhees).

1359-6454/$30.00
doi:10.1016/j.actamat.2005.12.038

The difficulty in developing such a theory lies in the need to account for the overlapping diffusion fields surrounding the particles. Because of this, most theories assume that the particles are spherical and noncontacting, which limits most theories to small volume fractions ($\lesssim 0.3$), with the notable exception of the effective medium theories [8,9,14].

Experimental aspects of coarsening in the solid–liquid system have been limited as well. The characterization of the microstructures for comparison to theory has been mainly confined to high volume factions of coarsening phase using two-dimensional (2D) sections [15–20]. However, recent experiments [21–23] performed as part of the coarsening in solid liquid mixtures (CSLM) project, a microgravity experiment performed on the space shuttle on missions STS 83 and STS 94, investigated the kinetics and microstructural evolution of Sn-rich particles dispersed in a Pb–Sn eutectic liquid matrix over a wide range of volume fractions. At low volume fractions a reasonable agreement between coarsening simulations, but not coarsening theory, and experiment was obtained. The coarsening models make predictions for three-dimensional (3D) systems, thus the comparison between theory and the data taken from 2D plane sections requires that the 3D predictions of theory be recast to make predictions of the microstructure that can be measured on 2D plane sections [24]. This was done assuming that the particles are spherical, an approximation that is valid only at low volume fractions where there are few particle–particle contacts.

In contrast, at higher volume fractions there was a significant disagreement between the predictions of mean field coarsening theory and the results from the experiment [22,23]. These discrepancies were mainly attributed to the increased number of particle contacts that occur at a high volume fraction of particles. However, the coordination number, C, defined as the number of particle–particle contacts per particle, could not be determined from 2D sections. Furthermore, the coordination number has been identified as an important microstructural parameter for microstructures with a high volume fraction of particles. For example, the nature of the particle contacts has been shown to affect the thermal expansion [25] and the mechanical properties of liquid phase sintered materials [26]. In addition, the number of grain faces in single-phase polycrystalline materials is also an important microstructural parameter for understanding the microstructural evolution [27,28]. One can measure the number of contacts per particle using a 2D plane section, but in order to convert this information to the 3D coordination number, one must assume that the particles are spherical and either monodisperse [29], or make assumptions about the dihedral angle and the 3D particle size distribution [30,31]. Thus, only by obtaining 3D data, can one avoid the many assumptions and approximations inherent in interpreting measurements made on 2D sections and achieve a more direct comparison to theory.

Within the last 10 years, there has been a dramatic increase in the amount of 3D data published in materials science investigations [27,32–38]. This has been due mostly to advances in computational power and software development, but also due to new experimental techniques for collecting 3D data. Several of these investigations have concentrated on microstructural evolution during grain growth [27,36]. Liu et al. investigated the 3D grain structure of an austenitic steel alloy using serial sections, with more than 1000 grains sampled. They found a near-linear relationship between the number of faces per grain and the spherically equivalent radius of the particle. Krill and Chen [39] analyzed a large volume of grains in Al–Sn system using X-ray microtomography. They found reasonable agreement with phase-field grain growth simulations, but poor agreement with more common 3D Poisson–Voronoi tessellation, which is often used to describe grain structures. Grain growth is similar to particle coarsening in that the overall energy of the system is lowered by reducing the total interfacial area, and it can be viewed as the limit of 100 vol.% coarsening phase. However, grain growth occurs in a single phase system, and the kinetics of the process are controlled by diffusion of atoms across a grain boundary, giving rise to a different temporal exponent of 1/2 for the average grain size, and to a different steady-state grain-size distribution.

To the best of our knowledge, there has been only one other investigation of the 3D microstructure of a large set of particles dispersed within a liquid matrix. Tewari et al. [37] used serial-sectioning to analyze the 3D microstructure of a liquid-phase sintered 83 wt.% W–Ni–Fe alloy under varying gravitational conditions. They measured both the particle size distribution and the particle–particle contact distribution for samples sintered in normal gravitational conditions and sintered in a microgravity environment. By montaging many 2D images into one continuous section, they could create a large 3D volume. However, because the height of the analyzed volume was relatively small compared to the particle diameter, many of the particles intersected the outside walls of the analyzed volume, which significantly limited the total number of particles that could be fully analyzed. Interestingly, they found that, when normalized to the average number of contacts per particle, the contact distribution was invariant with the gravitational environment present during the sintering process. In addition, it was found that the number of contacts per particle was proportional to the square of equivalent particle radius.

In this investigation, we will present the analysis of the 3D structure of coarsened Sn-rich particles dispersed in a Pb–Sn eutectic matrix over a range of volume fractions. Sedimentation of the particles at lower volume fractions is avoided by processing the samples in a microgravity environment, as part of the NASA CSLM project. A method of efficient serial sectioning is used to collect a statistically significant number of particles (>1000) for each volume fraction. Using these sections, the 3D microstructure is reconstructed and the particle sizes and number of contacts per particle are measured. Furthermore, using

microstructural simulations we will also examine the effect of the particle size distribution and volume fraction on the particle contact structure.

2. Experimental method

We examine two volume fractions. The first volume fraction, containing approximately 78 vol.% Sn-rich particles was coarsened in a ground-based laboratory. Due to the large density difference between the Sn-rich particles and the Pb–Sn liquid, the particles sediment quickly and form a stable network of particles, or particle skeleton, within the liquid matrix. For this system, a stable particle skeleton forms at a volume fraction of $\lesssim$80 vol.%, and thus there was little sedimentation. The second sample was coarsened as part of the CSLM project, and had a volume fraction of 52 vol.% solid. To avoid the particle sedimentation, the heat treatments were performed in a microgravity environment aboard the Space Shuttle Columbia on STS-83 and STS-94. Two-dimensional analyses of samples processed on these flights have been previously performed [21–23,40]. However, in order to obtain the microstructural characteristics, such as the particle contact structure, the 3D microstructure was determined using serial sectioning and 3D reconstruction.

Traditional 3D serial sectioning is an extension of 2D sectioning techniques, where sequential 2D sections that are closely spaced are imaged, then aligned and stacked using a computer program, generating a 3D structure [32,35]. In the method of serial-sectioning originally developed by Alkemper and Voorhees [35], the sectioning machine and microscope are integrated so that each 2D section can be imaged without removing the sample from the mount. This eliminates the need for fiduciary marks since any rotational misalignments are negligible, and only the translational misalignment caused by moving the sample between the microscope and the micromiller areas must be measured. The translational misalignment is determined to an accuracy of <0.5 μm. The images obtained are then stacked into a 3D array by using the measured misalignments, creating a reconstruction of the 3D microstructure.

Serial sections were taken from each sample using this method. The optical resolution of the images in the 2D sections was 1.1 μm for both the 78 vol.% sample and the 52 vol.% samples. The distance between two consecutive sections, or the section height, was chosen so that the there were approximately 20 sections over an average particle diameter. The section heights were 6.65 μm for the 78 vol.% sample and a 4.75 μm for 52 vol.% sample. This sets the resolution of the reconstruction in the sectioning direction.

Before the 3D structure can be graphically rendered from the data, the location of the interfaces between the solid particles and the liquid matrix must be determined. This is achieved by thresholding the images so that each pixel belonging to the particle phase is set to white (or a value corresponding to white), while each belonging to the matrix phase is set to black.

Because there is no contrast between the particles at the particle–particle contacts (see Fig. 1), the particle–particle interface cannot be determined simply by processing the image. In a two-dimensional analysis, it would suffice to draw a separating segment between two contacting particles. However, since the 2D images obtained herein are reconstructed into 3D structures, such a method would result in unsegmented particles when the boundaries are nearly parallel to the sectioning direction. In order to detect boundaries between contacting particles in three dimensions, we implement a 3D watershed segmentation algorithm.

The watershed technique provides a method for segmenting contacting particles in three dimensions, as well as uniquely labeling each particle so that the particle can easily be identified for further analysis. The watershed segmentation of microstructures was first proposed by Digabel and Lantuájoul [41]. The watershed method is best understood in terms of geography, where a watershed is defined as the line of division between two adjacent

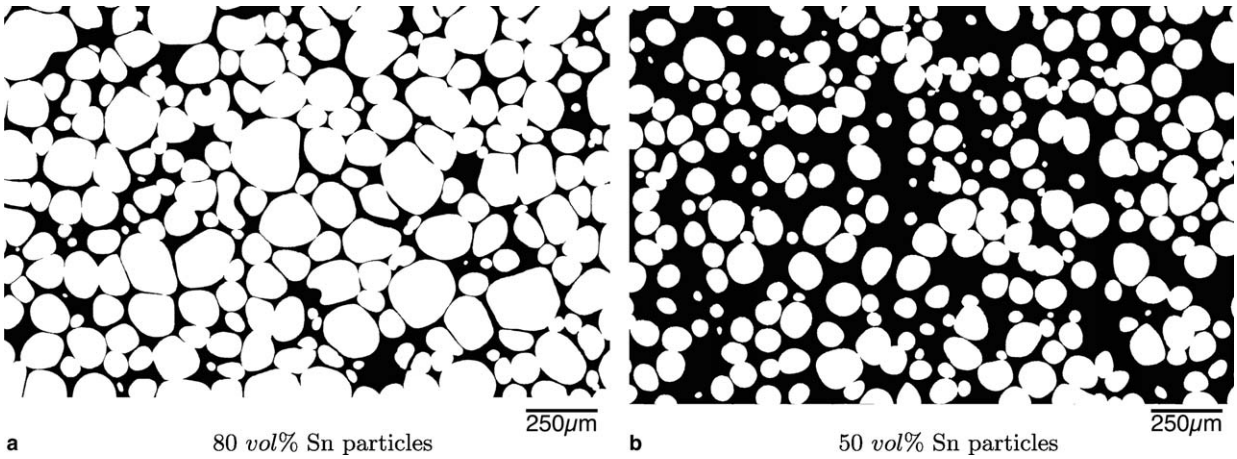

Fig. 1. Representative 2D sections of the microstructures after 9500s of coarsening at (a) 78 vol.% and (b) 52 vol.%.

drainage basins, so that a drop of water on one side of the watershed segmentation line flows downward to one basin, and a drop of water on the other line flows downward to the other basin.

Fig. 2 shows an example of how the watershed algorithm segments joined particles. For clarity the example is presented in 2D, however the algorithm is easily extended to three dimensions. In order to use the watershed method to segment the particles, the volume (or in the case of 2D, an image) needs to be transformed so that each particle acts as an individual basin. This is done by constructing a Euclidean distance map of the volume, so that the value at each element of the array, or pixel, is the minimum distance to the solid–liquid interface, as shown in Fig. 2(b). Here, the distance from a pixel inside a particle to the interface is defined as a negative distance, and the distance from a matrix pixel is a positive distance. This creates a virtual basin for each particle with a minimum near the center of the particle, and also creates virtual ridges along the particle–particle contacts.

Because the distance function either continuously increases or decreases (the function does not contain any flat steps or terraces), we can implement a simple rainfalling watershed [42]. The algorithm simulates the motion of a raindrop, first placing it at a pixel, then allowing the rain drop to flow downhill until it reaches the minimum height of the basin (a collection point), which has an associated identifier, as illustrated in Fig. 2(b). The original pixel, as well as any pixels along the downhill path are then labeled with the unique identifier (Fig. 2(c)). This process is repeated at each pixel belonging to the particle phase. The downhill motion of the drop is simulated by moving the drop to the nearest neighbor minima. If the drop is at the minimum value for the nearest neighbor box, it is assumed that the drop is at a basin minima and the path is labeled with a new unique identifier. If the surface contained any steps, or terraces, the nearest neighbor minima would not be sufficient to determine whether or not the drop had reached the bottom of a basin. There are many other watershed algorithms that address this problem, but they are unnecessary for this work (for a more complete review of watershed algorithms see the review by Roerdink and Meijster [43]).

The largest error associated with the watershed technique is over-segmentation, wherein a particle is incorrectly separated into two or more regions. Over-segmentation

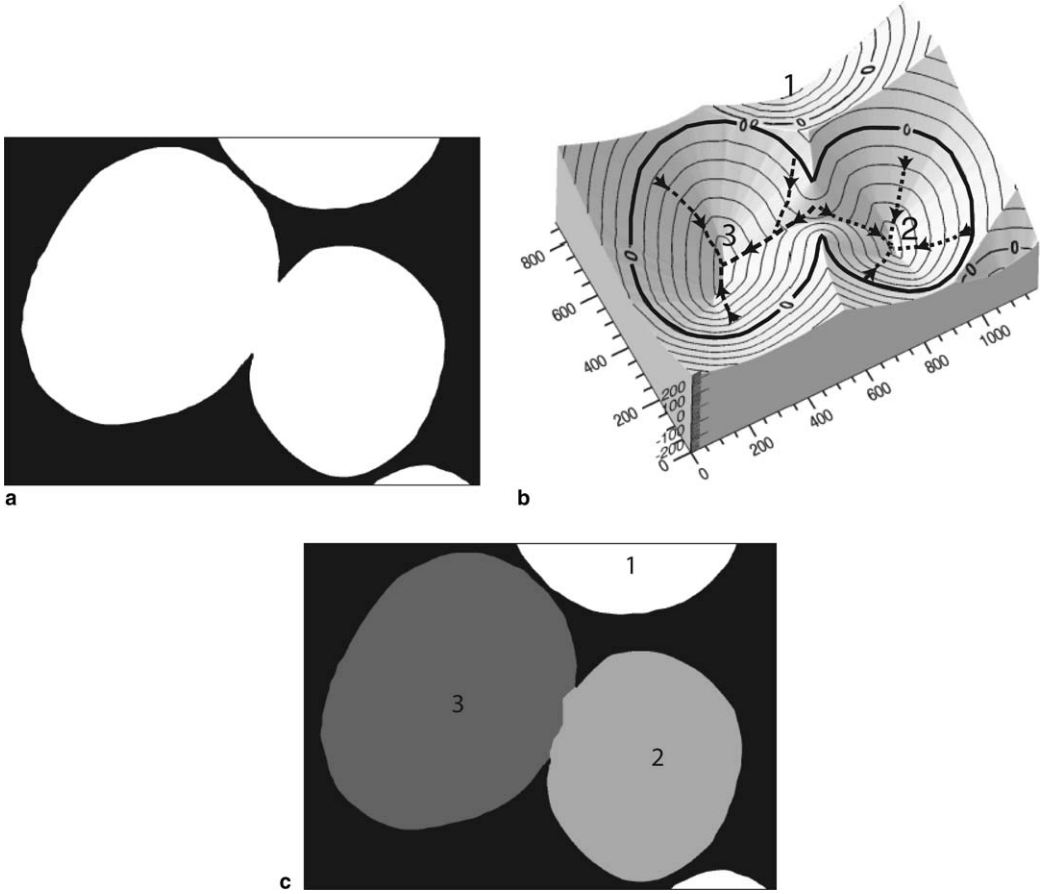

Fig. 2. Two-dimensional example of the rainfalling watershed segmentation. (a) Binary image of the particles before segmentation. (b) Surface plot of the 2D Euclidean distance map, where each point is equal to its distance from the interface making each particle a basin. Several example rainfalling simulations are displayed, showing how the simulated raindrops collect in each of the particle basins. (c) All the rainfalling points that collect in the same basin are labeled with a unique identifier for that basin, effectively segmenting the particles.

occurs when the shape of the particles deviates from a perfect circle (or sphere in the 3D case), causing multiple minima within one particle. The over-segmentation can be greatly reduced by smoothing the distance map to remove noise near the bottom of the basins, thus smoothing over multiple closely spaced minima. We implemented a box average smoothing of the distance map to reduce the fluctuations near the bottom of the basins. To further reduce over-segmentation, we proceed as follows. The value of the distance map at the identifying minimum is given approximately by the radius of the particle. Thus, one would not expect to find another minimum within that distance. If another minimum is found within the value of the distance function at the minimum of the particle, the two regions can be safely combined into one particle region.

Since the watershed segmentation is fully automated and does not require user intervention, it allows for a large number of particles to be segmented and analyzed quickly. With each particle uniquely identified, the position and the particle size of each particle can easily be determined. Here, we use the center of mass for the position of the particle, and the spherically equivalent radius for the particle size. Since particles near the edge of the sampled volume may intersect the edge, they need to be removed from the analysis. However, simply removing particles that contact the edge of the analyzed volume would bias the results toward smaller particles, which are less likely to intersect the edge than larger particles. Thus, a guard frame with a thickness of 1.5 times the average particle radius is constructed around the sample. Any particle that has a center-of-mass position in the guard frame is removed, thus removing edge effects in an unbiased manner.

The number of contacts per particle can be obtained by counting the number of unique regions that directly neighbor a given particle region. Only particles that are not eliminated by the guard frame can act as the primary particle, or contacted particle. All the particles in the analyzed volume, including those that are within the guard frame, can act as a secondary, or contacting particle. Any thin liquid films that form between the particles that have a width less than the resolution of the reconstruction will also be counted as a contact. As mentioned before, the resolution of the reconstruction is 1.1 μm in the section plane, and the section height sets the resolution in the third direction. The segmentation of the particles and analysis is computer automated, eliminating the need for human intervention, and thus is capable of generating a large amount of statistics in a relatively short time in an unbiased fashion.

3. Results and analysis

The 3D reconstruction of the high-volume-fraction sample processed on earth is shown in Fig. 3. The total volume of sample analyzed is 1.35 mm × 1.94 mm × 1.00 mm, reconstructed from 150 sections. One thousand one hundred and seventy particles are analyzed after the removal of those in the guard frame. The measured volume fraction

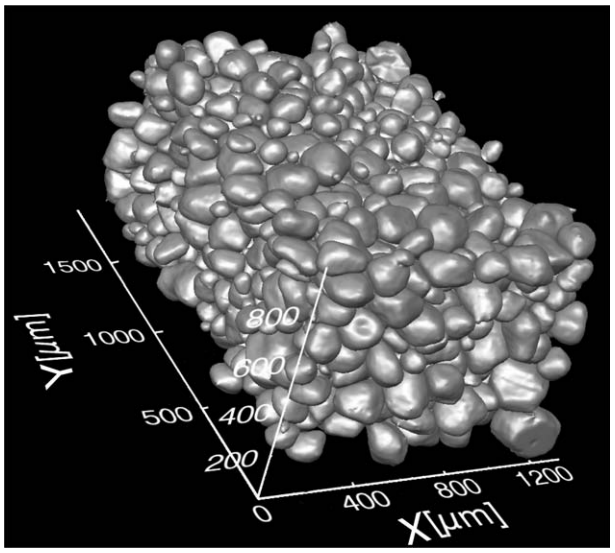

Fig. 3. A 3D reconstruction from serial sections of 78 vol.% Sn particles within a Pb–Sn eutectic matrix after 9500s of coarsening. The Pb–Sn eutectic matrix has been made transparent so that the particles can be viewed.

of the analyzed volume is 78 vol.%, and the average particle radius is 57.8 μm. The reconstruction shows that at this high volume fraction the particles are irregularly shaped, but are still approximately equiaxed. The gravitational direction is along $\hat{\mathbf{y}}$. The particles do not show any particular deformation in this direction, indicating that the gravitational force is not significant enough to deform the particles, although it is enough to cause their sedimentation.

The normalized particle size distribution (PSD) is shown in Fig. 4. Two theoretical predictions are overlaid for comparison. The first is from Marsh and Glicksman [14], which is a mean-field theory for coarsening at various volume

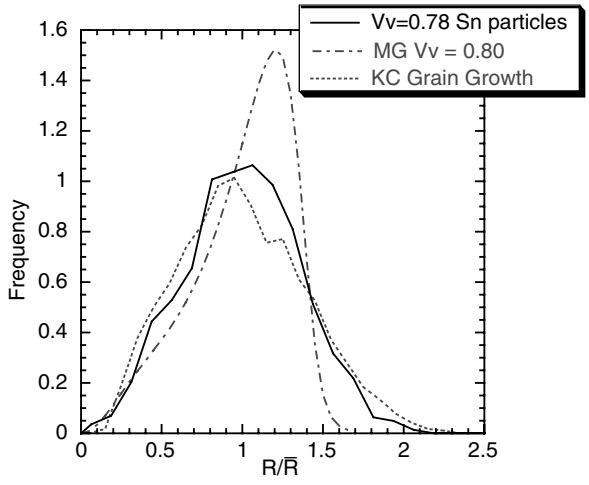

Fig. 4. Normalized particle size distributions for 78 vol.% Sn particles after 9500s of coarsening. Also plotted are the Marsh and Glicksman particle coarsening theory (MG) [14] and the results from grain growth simulation by Krill and Chen (KC) [39].

fractions. This is one of the few particle coarsening theories that make predictions at high volume fractions ($V_V > 0.5$). There are significant disagreements between this theory and the experimental results. This discrepancy is most likely because, while the MG theory makes predictions at higher volume fractions, the theory does not account for the particle–particle contacts and shape distortions needed to fill space at higher volume fractions. As a particle begins to contact other particles, the contacts create a flat surface, and thus the interface must possess regions of high curvature to enclose the particle, as seen in Fig. 5. The flat surface does not contact the liquid matrix, and therefore the flat surface does not have a diffusional interaction with the other particles, which lowers the effective area of the particle. The high curvature regions do contact the liquid phase and the high curvature regions do have a diffusional interaction with the other particles through the liquid matrix. This means that a larger particle with a high number of contacts will appear to expose a higher curvature to other particles than is represented by the volume equivalent radius. We hypothesize that it is this increase in the effective curvature that stabilizes the larger particles in the tail of the PSD at high volume fractions. As the volume fraction increases, the number of the particle–particle contacts and the shape distortions will increase, leading to a larger discrepancy.

The second comparison is with a phase-field simulation of grain growth from Krill and Chen [39]. In this model, grain growth occurs in a single phase material in which the grain boundary energy is assumed to be isotropic. This case can be considered equivalent to the limit of particle coarsening at 100 vol.% of coarsening phase. The normalized particle size distribution for the grain growth simulation is in better agreement with the experimental results. However, there are some small discrepancies between the two PSDs, especially at larger particle sizes. The PSD of the grain growth simulation has a lower peak hight and is broader than the PSD of the experiment.

Fig. 6 shows the reconstruction of the 52 vol.% sample processed in a microgravity environment. The total sample size analyzed was $1.65\ \text{mm} \times 1.950\ \text{mm} \times 0.760\ \text{mm}$, and was obtained using 160 sections. Note that the total sample volume collected is larger than what was collected for the high-volume-fraction sample due to improvements in the optical system that increased the size of the sampled areas in the 2D sections. The measured average particle size is 44.6 μm with 1808 particles analyzed. The reconstruction shows that the particle shape is much more spherical compared to those in the higher-volume-fraction sample. Due to a lower volume fraction, this sample has much more space between particles, leading to a longer characteristic diffusion distance and a longer diffusion time scale. Since coarsening is mediated by diffusion between particles, this explains the smaller average particle size compared with that of the higher-volume-fraction sample at the same coarsening time.

Fig. 7 shows the normalized PSD for the 52 vol.% sample. Overlaid are the PSDs for the 78 vol.% and the grain-growth phase-field simulation discussed earlier. We see that the 52 vol.% PSD is narrower than that of the 78 vol.% sample and that of the grain growth simulation. This is consistent with 2D experimental measurements as well as particle coarsening theories at lower volume fractions, which concluded that the PSD will become shorter and broader as the volume fraction increases [4,14,21,40]. However, there is still considerable disagreement in the overall shape of the distribution between the experiment at 52 vol.% and the predictions of particle coarsening theory. We also observe that the peak of the PSD moves toward

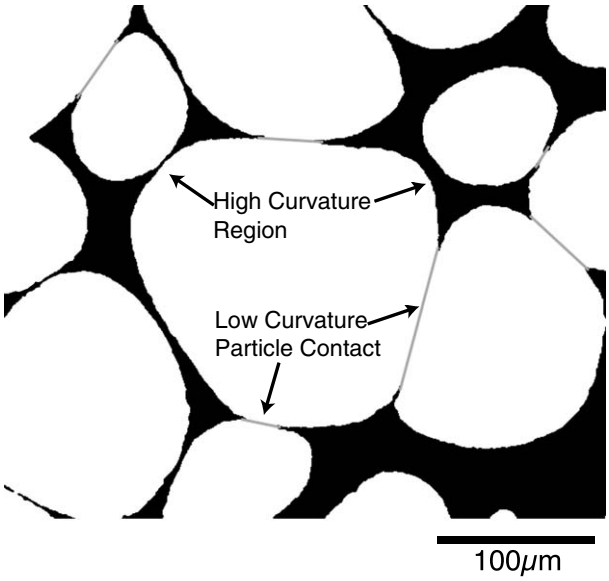

Fig. 5. Micrograph of $V_V = 0.78$ sample at 9500s of coarsening time, showing the difference in curvature at particle contacts and regions neighboring contacts. The gray lines representing particle contacts have been added for clarity.

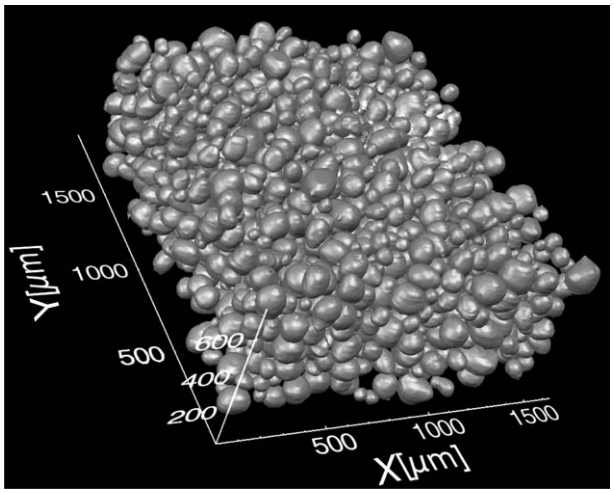

Fig. 6. A 3D reconstruction from serial sections of 52 vol.% Sn particles within a Pb–Sn eutectic matrix after 9500s of coarsening. The Pb–Sn eutectic matrix has been made transparent so that the particles can be viewed.

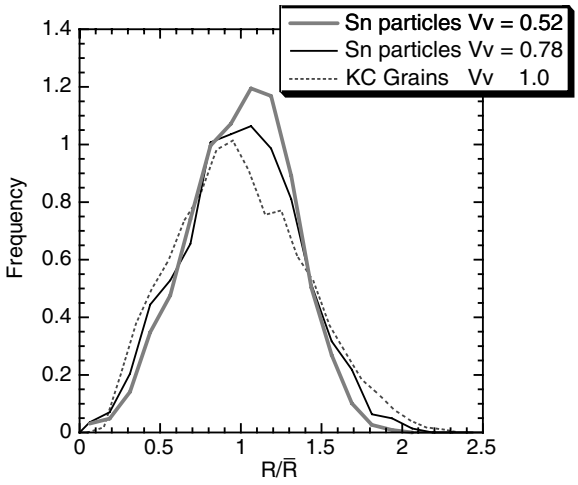

Fig. 7. Normalized particle size distributions for 52 vol.% Sn particles after 9500s of coarsening. For comparison the experimental results for 78 vol.% Sn particles and the phase-field results (KC) are also plotted [39].

lower normalized particle sizes as the volume fraction increases. This behavior has also been observed in experiments that employ measurements made on 2D sections, as well as in 2D phase-field simulations of particle coarsening [44], but is not well represented in most particle coarsening theories [8,14,45]. In addition, the trend that the slope of the tail of the PSD increases as the volume fraction decreases continues at 52 vol.%.

In grain growth, the numbers of grain faces, edges, and vertices are important measures in characterizing microstructures. In the particle coarsening system, particle edges and vertices are not easily defined. However, the number of particle–particle contacts, C, is analogous to the number of grain faces, F, and in the limit of 100 vol.% coarsening phase these two measures are equal. The number of particle–particle contacts is measured for each particle within the unbiased sample volume. In Fig. 8 we show several particles with their contacting neighbors. We can see from these images that the number of contacts is a function of the particle size of the primary particle. This relation is shown more clearly in Fig. 9, where $C/\bar{C}$ is plotted as a function of $(R_C/\bar{R})^2$ for the two volume fractions. Tewari et al. [37] suggest that it is reasonable for the normalized number of contacts, $C/\bar{C}$, to be proportional to the surface area of the primary particle and thus is given by:

$$C/\bar{C} = (R_C/\bar{R})^2 \tag{1}$$

where R_C is the average particle radius with a given number of contacts. While this equation seems to describe their data well, it is unclear if this should be the case for other systems as well.

Fig. 9 shows that the 52 vol.% sample does display the linear functionality predicted by Eq. (1), but the slope of the line is less than one. The normalized number of contacts in 78 vol.% sample clearly is not linear with the square of the normalized average particle size. We see that smaller particles have a larger number of contacts than expected from this equation. It appears that, at larger values of $R_C/\bar{R}$, the normalized number of contacts does follow a linear trend, but again the slope is less than one.

Fig. 10(a) shows the distribution of contacts, C, for the 78 and 52 vol.% samples. We have also included the distribution of grain faces, F, from the grain growth simulation, which is analogous to C in the particle coarsening system.

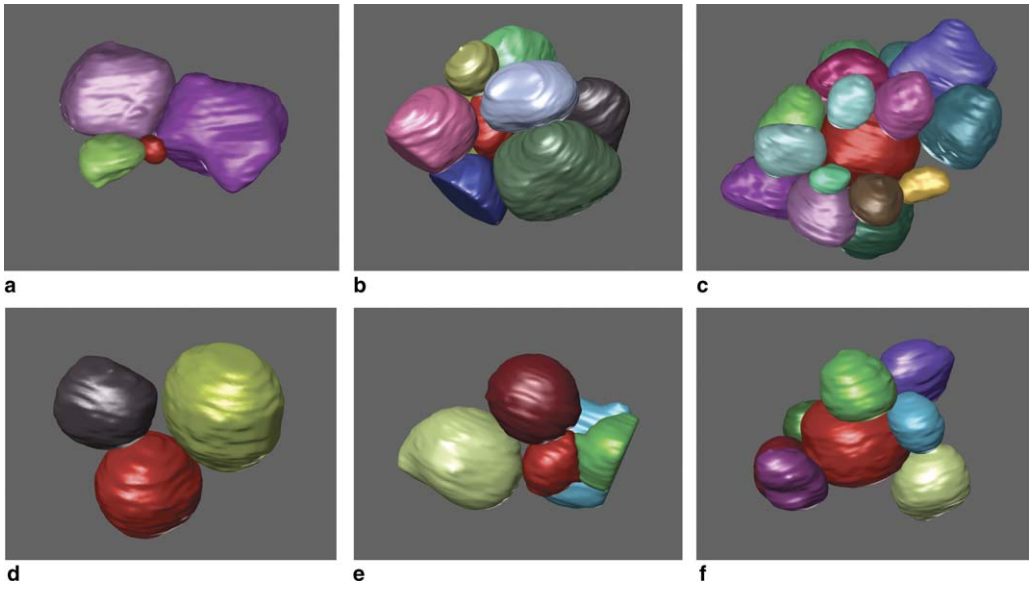

Fig. 8. Reconstructions of contacting particles. The center particle is colored red for all of the reconstructions, the contacting particles are randomly colored. Images (a)–(c) are from the 78 vol.% sample, images (d)–(f) are from the 52 vol.% sample. (a) 25 μm radius particle with three contacting particles. (b) 53 μm radius particle with eight contacts. (c) 110 μm radius particle with 20 contacts. (d) 49 μm radius particle with two contacting particles. (e) 37 μm radius particle with four contacts. (f) 74 μm radius particle with eight contacts. Also evident is that the particles at 52 vol.% tend to be more spherical than those at 78 vol.%.

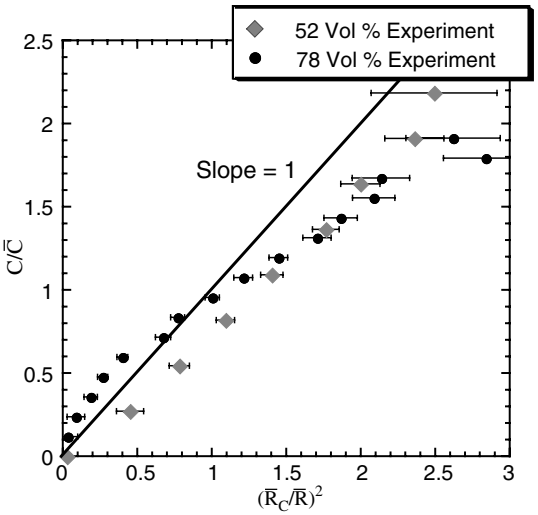

Fig. 9. The normalized number of contacts versus the square of the scaled particle average radius with the given number of contacts, $\bar{R}_C$. The error bars are the standard error in the scaled radius.

It is evident that the volume fraction has a dramatic effect on the connectivity of the system. The average number of contacts increases more than twofold, from 3.66 for 52 vol.% to 8.36 for 78 vol.%. In addition, the distribution becomes much broader as the volume fraction increases. We note that for the 78 vol.% sample every particle has at least one contact. This is expected since the sample was coarsened under normal gravitational conditions, causing sedimentation of the particles. However, even the 52 vol.% sample, which was coarsened in a microgravity environment in an effort to eliminate sedimentation, has only seven free-floating particles, a small number considering that over 1800 particles were analyzed.

The normalized contact number distribution is presented in Fig. 10(b). The result shows that there is good agreement between the normalized particle contact distributions at the two different volume fractions. The two normalized contact distributions also agree reasonably well with the distribution for the normalized number of faces from the grain growth simulation for $C/\overline{C} > 1$, and the disagreement is only significant at lower contact numbers, $C/\overline{C} < 1$. The difference stems from the fact that grain growth requires the particle phase to fill space, and thus, assuming flat grain faces, each grain must have at least four faces. With the particle microstructure there is no such limitation, therefore less than four contacts is allowed. Despite this difference, the agreement between the contact distribution measured at 80 vol.% and the number of faces during grain growth is very good for almost all $C/\overline{C}$.

While the phase-field simulation of grain growth appears to describe the PSD of the experimental data well, the kinetics of grain growth and particle coarsening are very different. During particle coarsening the kinetics are controlled by the diffusion of material from smaller particles to larger particles through the matrix, thus increasing the average particle size over time. Coarsening theory [2,3] shows that the average particle size, $\overline{R}_{PC}$, will increase with time, t, as described by a power law:

$$\overline{R}_{PC}(t) = (K_{PC}(V_V)t + \overline{R}_{PC}(0)^3)^{1/3} \quad (2)$$

where K_{PC} is the particle coarsening rate constant, which is a function of the volume fraction, V_V, of the coarsening phase, and $\overline{R}_{PC}(0)$ is the average particle size at $t = 0$.

On the other hand, the kinetics of grain growth are controlled by a very different process, where growth or shrinkage are mediated by atoms jumping across the grain boundary interface. Traditional grain growth theory [46,47] predicts that the average grain size, $\overline{R}_G$, is given by

$$\overline{R}_G(t) = (K_G t + \overline{R}_G(0)^2)^{1/2} \quad (3)$$

where K_G is the grain-growth rate constant. Unlike particle coarsening, K_G is not a function of volume fraction since, by definition, grain growth occurs in a single phase system,

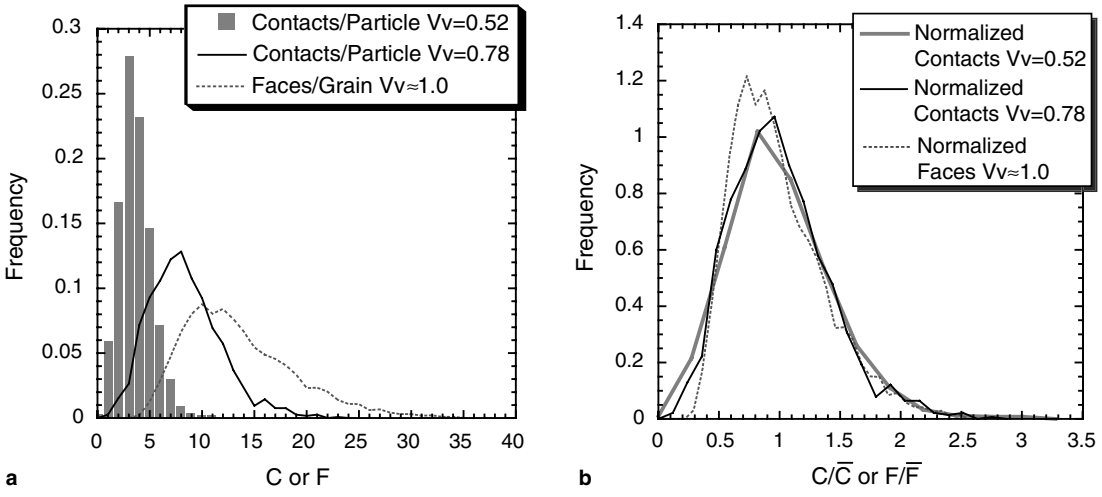

Fig. 10. (a) Distribution of the number of contacts, C (or faces, F for grains) per particle. (b) Normalized contact distribution where the distribution is scaled to the average number of contacts for the system.

i.e., 100 vol.%. Krill and Chen show that their simulation result follows the grain growth law, $\overline{R}_G \propto t^{1/2}$.

One of the objectives of the CSLM project was to compare the kinetics of the particle coarsening with theoretical predictions. This was achieved by determining the average particle size as measured on plane sections as a function of coarsening time for a variety of volume fractions [21,23,40]. These studies showed that the average particle radius was proportional to $t^{1/3}$ for all volume fractions including 50 and 80 vol.%. Thus, we conclude that the kinetics of the systems considered here are consistent with a diffusion-limited coarsening process.

However, the PSD and the contact distribution at 78 vol.% are very close to those for grain growth. It is unclear whether the similarity in the normalized contact distributions from the two experiments and the phase-field model for grain growth is a consequence of the microstructural evolution processes, or is a result of packing a polydisperse set of particles to a particular volume fraction. Therefore, we simulate the random packing of polydisperse spheres within a volume by using the experimentally measured PSD. Since it is nearly impossible to place nonoverlapping polydisperse spheres at higher volume fractions ($\geqslant$50%), it is necessary to allow the spheres to overlap. We use the extent of the overlap as an input parameter. In this simulation, the spheres are randomly placed in space, starting with the largest particle bin in the given PSD and ending with the smallest. This bin-by-bin placement is necessary to place particles with as little overlap as possible at high volume fractions where the amount of free volume is limited.

A user defined overlap parameter, f, sets the maximum amount of overlap allowed between two particles as follows:

$$\begin{aligned} d_{ij} &> (1-f)r_i + r_j \quad \text{for} \quad r_i < r_j \\ d_{ij} &> r_i + (1-f)r_j \quad \text{for} \quad r_i \geqslant r_j \end{aligned} \tag{4}$$

where d_{ij} is the distance between the centers of spheres i and j, and r_i and r_j are the radii of spheres i and j. This criterion, in which the maximum overlap distance is given by a fraction of the smaller particle, prevents the smaller particle from being placed entirely within the larger particle. To account for the overlapping volume that occurs when two particles contact, the overlap volume is subtracted from the original particle volume. The spherical equivalent radius is then calculated based on this corrected volume. This spherical equivalent radius is then used to calculate the volume fraction of particles, and the PSD of the simulations. Thus, there can be small differences between the input PSD and the final PSD, depending on the allowed amount of particle overlap in the simulations. Fig. 1(b) shows that the dihedral angle formed between Sn-rich particles is small for the Pb–Sn system. Therefore, we assume that all the boundaries in the system are wetted (or equivalently that the dihedral angle is equal to zero), and that the particle overlap approximates the shape distortions needed to accommodate the desired volume fraction. Therefore, we choose to minimize the overlap parameter while achieving a simulated microstructure. Using the smallest possible overlap has the added advantage of causing the smallest amount of change between the input PSD and the resultant PSD. This minimum overlap threshold was determined by iteratively constructing microstructures with decreasing overlap parameters until the simulation could not reach the desired volume fraction with a large number of attempts create the microstructure.

Table 1
Minimum overlap parameter needed to create a simulated microstructure and the resultant average number of contacts per particle

Microstructure	Minimum f	$\overline{C}$ per particle
52 vol.% Experiment	N/A	3.66
78 vol.% Experiment	N/A	8.36
100 vol.% Phase field simulation	N/A	13.7
52 vol.% Random simulation	0.0	0.00
66 vol.% Random simulation[a]	0.18	4.72
66 vol.% Random simulation[b]	0.18	4.46
78 vol.% Random simulation	0.32	6.79
78 vol.% Monodisperse simulation	0.51	6.99

[a] Simulated 66 vol.% using the PSD from the 52 vol.% experiment as input.
[b] Simulated 66 vol.% using the PSD from the 78 vol.% experiment as input.

Table 1 lists the volume fraction, minimum overlap fraction achieved, and the resultant average number of contacts per particle for the random simulated microstructures, and Fig. 11 shows representative cross-sections of the simulated microstructures. Notice that the minimum overlap needed to create a 52 vol.% microstructure is zero (Table 1). This means that a random structure, with this particle size distribution, can be constructed so that no particle touches another particle. Packing theory has shown that for loose random packing of monodisperse spheres the maximum volume fraction that can be achieved is approximately 56 vol.% [48]. While the structures considered here have a polydisperse particle size, we find that this volume fraction was approximately the same for the zero-overlap maximum packing limit. The results show that there are a significant number of contacts within the experimental microstructure. We believe that this discrepancy arises from local clustering of the particles in the experimental sample. Close examination of the 2D sections from the simulations (Fig. 11(c)) and the 2D section from the experiment (Fig. 1(b)) shows that while the overall volume fraction of the experiment is comparable to the 52 vol.% simulation, the local contact structure around a particle is similar to that in the 66 vol.% simulation.

This qualitative observation of clustering can be quantified by measuring the pair correlation function (PCF). The PCF is defined as the ratio of the number of particle centers per volume averaged over a spherical shell of radius x and thickness dx around a particle to the total number of particles per unit volume:

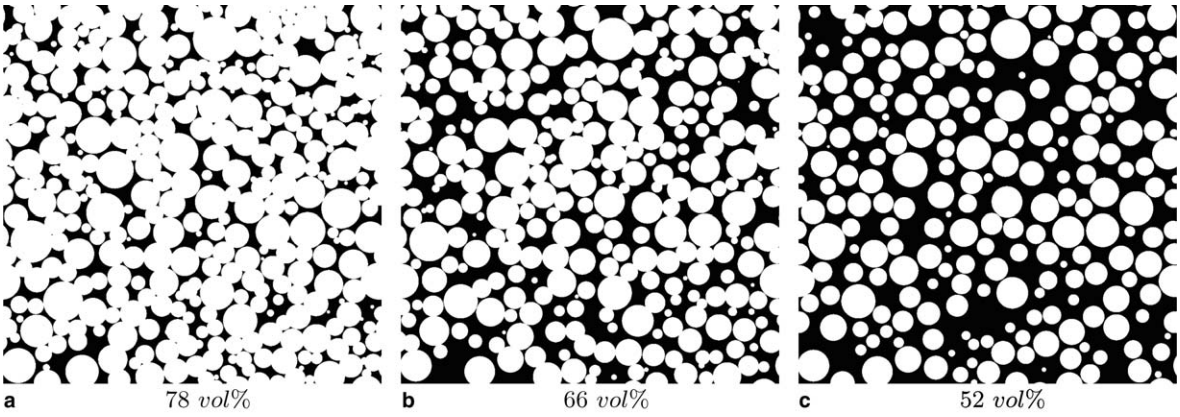

Fig. 11. Two-dimensional sections of the simulated microstructure at (a) 78 vol.%, (b) 66 vol.%, and (c) 52 vol.%

$$G(x) = \frac{N_V \text{ in a shell of radius } x \text{ to } x + dx}{\overline{N}_V} \quad (5)$$

where N_V is the number of particles per volume and $\overline{N}_V$ is the total number of particles per volume. For any structure that does not have a long range order, $G(x) \to 1$ as $x \to \infty$. In order to compare the simulation and experimental microstructures, the PCFs are normalized to the average particle radius.

The normalized PCF for the 52 vol.% sample is shown in Fig. 12. The primary peak for this structure is located at less than $2\overline{R}$ indicating that, on average, the distance between two neighboring particles is less than the sum of the radii of two average-sized particles. The PCFs for the 52 and 66 vol.% microstructure simulations are also plotted in Fig. 12. It is clear that the location of the primary peak differs significantly between the 52 vol.% simulation and the experiment. In contrast to the experiment, the simulation results show the primary peak is greater than $2\overline{R}$. This indicates that locally the particles are closer to each other in the experiment than in the simulation where particles are randomly placed. Therefore, the particles in the experimental sample are not randomly distributed, but rather clustered. Fig. 12 shows that the position of the primary peak is consistent with a random spatial distribution of particles at a volume fraction of 66 vol.%. Thus, we will use the simulated 66 vol.% microstructure as an approximation of the local contact structure in the 52 vol.% structure. The average number of contacts for the 66 vol.% sample is 4.70, which is higher than what is measured for the 52 vol.% experiment. This is expected since the simulation only approximates the local clustered structure found in the experiment. Particles that are near the edge of a cluster will have a lower number of contacts than those in the middle, thus lowering the average.

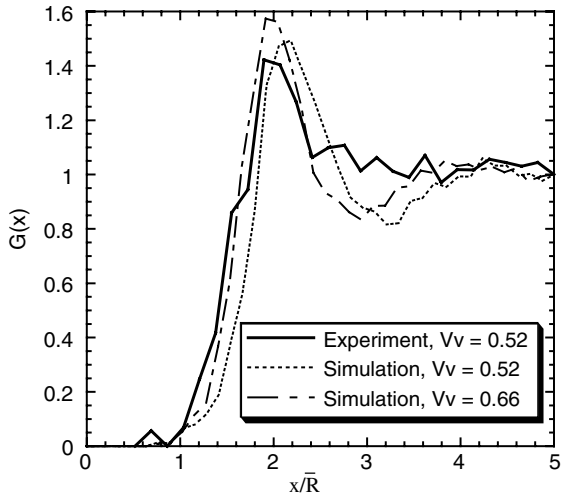

Fig. 12. The pair correlation function for the 52 vol.% experiment, and simulated random microstructures at 52 and 66 vol.%.

Fig. 13 shows the normalized contact distributions for the simulated microstructures and for comparison we have also included the normalized contact distributions for the experimental microstructures. Fig. 13(a) shows the normalized contact distributions for the simulations at 78 vol.%. We find that there is relatively good agreement between the simulations at 78 vol.% and the experimental results at the volume fraction. Notice, however, that the normalized contact distribution for the simulated microstructure is slightly shifted to left as compared to the experimental results. Also, as shown in Table 1, the simulated average number of contacts for this volume fraction is somewhat lower than in the microstructures that were measured experimentally. One reason for this discrepancy is that the experimental particles are deformed and are irregularly shaped. It has been shown that for hard mono-disperse ellipsoids the average packing fraction and number of contacts is higher than what is found for hard sphere packing [49]. Fig. 11(a) shows a 2D section of the 3D simulated microstructure. It shows that the overlap parameter only approximates the shape distortions and does not reproduce the anisotropically deformed particles that are often observed in the real microstructure seen in Fig. 1(a). In addition, the simulation has a near perfect resolution for determining whether two particles contact, with the only limit being the numerical machine precision. However, as mentioned in Section 2, the 3D reconstructions have a

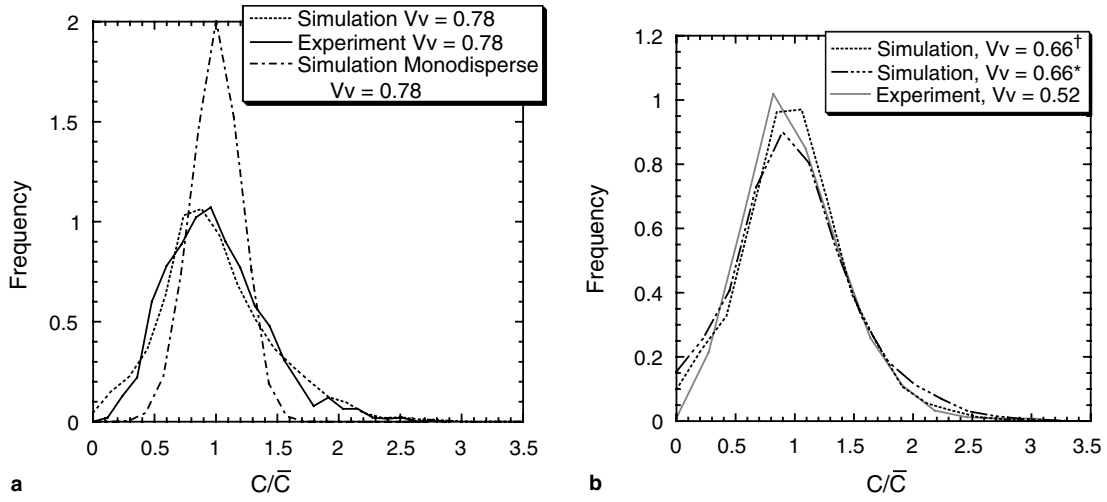

Fig. 13. (a) Normalized contact distributions for the 78 vol.% simulation, created using the PSD from the 78 vol.% and the normalized contact distribution for a simulated microstructure at 78 vol.% using monodisperse particle size. Also plotted is the normalized contact distribution for the 78 vol.% experiment. (b) Normalized contact distributions for the simulated and experimental microstructures. †Simulated 66 vol.% using the PSD from the 52 vol.% experiment as input, and *simulated 66 vol.% using the PSD from the 78 vol.% experiment as input. Also plotted is the normalized contact distribution for the 52 vol.% experiment.

finite resolution, with the poorest resolution being in the sectioning direction. This would give rise to an overestimation of the number of contacts in the experimental measurements. We believe that the shape deformity and experimental resolution fully explain the differences between the experimental and simulated results.

Also plotted in Fig. 13(a) is the contact distribution for a monodisperse PSD (i.e., the radius of the particle is fixed to a single value). There are dramatic differences in the shape of the distribution, although the average number of contacts for the monodisperse distribution is very similar to the polydisperse simulation (see Table 1). The normalized contact distribution is much narrower, and more symmetric than the distributions from the polydisperse systems. Thus, large changes in the shape of the PSD do have an effect on the contact structure. Furthermore, the invariance of the normalized contact distribution as a function of volume fraction during coarsening does not indicate that the contact distribution is unique for a given volume fraction of particles. The contact distribution is a function of the PSD; however, the small differences in the PSDs seen experimentally as the volume fraction changes are not large enough to significantly change the normalized contact distributions. To verify this, two microstructures were simulated at 66 vol.%; the first using the experimental 52 vol.% PSD as the input PSD and the second using the experimental 78 vol.% PSD as input for creating the simulated microstucture. We see little change in either the average number of contacts (Table 1) or the normalized contact distributions (Fig. 13(b)).

Fig. 13(b) also shows that the normalized contact distribution for the simulated 66 vol.% microstructure agrees well with the experimentally measured distribution for 52 vol.%. As mentioned above, because of clustering within the experimental microstructure, 66 vol.% was used as an approximation to the local structure in the experimental microstructure.

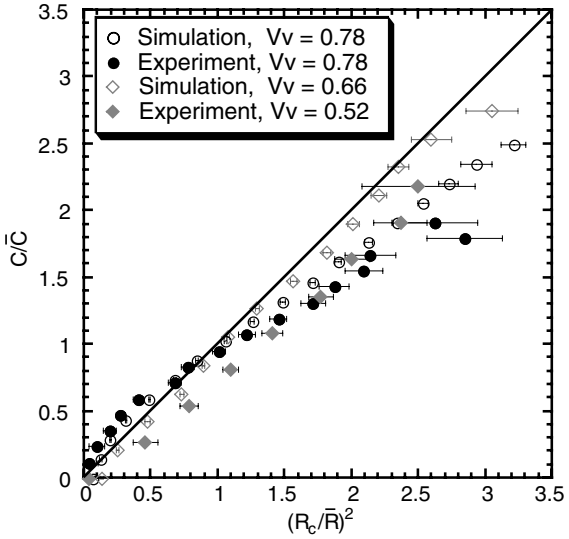

Fig. 14. The normalized number of contacts versus the square of the scaled particle average radius for 66 vol.% simulation, 78 vol.% simulation, 52 vol.% experiment, and 78 vol.% experiment.

Fig. 14 shows the normalized number of contacts as a function of the square of the normalized contact particle radius. The 66 vol.% simulation shows a linear relationship, and the slope of the line is approximately one. The difference in the slope between the experiment at 52 vol.% and the simulation at 66 vol.% most likely is due to the clustering that occurs in the experiment, where particles along the edge of a cluster would have a lower number of contacts, thus lowering the average for a given radius. Alternatively it may be due simply to the change in volume fraction between the experiment and the simulation.

Fig. 14 also shows that the simulation of the 78 vol.% microstructure agrees with the experiment, with the simulation duplicating the same nonlinear trend as observed in the experiment. There may be several reasons for this nonlinearity. The first maybe the nonspherical shape of the particles. In the simulations the nonspherical nature of the particles is approximated by the overlap. As the allowable overlap increases, the resulting particle shape will become less spherical. Another cause maybe a size–size correlation of the particles, so that smaller particles are more likely to be near larger particles and have a larger number of contacts. In the experiment a size–size correlation would be driven by the coarsening process. However, in the simulation, the size–size correlation is created by the method that is used to place particles in the simulation box. The smaller particles are the last particles to be placed in the volume, with the only remaining sites available for these small particles are the spaces formed between several larger contacting particles, which then establishes the size–size correlation in the simulation. In order to compare accurately the size–size correlations between the simulation and the experiment, one would require approximately 10 times more particles in the experimental volume to generate sufficient statistics.

It is important to note that, like the normalized contact distribution, the number of contacts as a function of particle radius is not a universal property of the packing of particles, and is not independent of PSD for the microstructure. For instance, for a monodisperse set of particles, there would be a vertical line on such a plot at $(R_C/\bar{R})^2 = 1$. Thus, the results from the microstructure simulations show that at high volume fractions of coarsening phase, it appears that the normalized particle contact structure is unique to a given PSD. It is critical to note that the physics that ultimately determine the shape of the PSD are dependent on the short range spatial arrangements of the particles, thus one cannot claim that during particle coarsening the contact structure is purely a function of the PSD, or that PSD is a function of the particle contacts; the two properties cannot be separated.

4. Conclusions

An efficient method of serial sectioning is used to analyze a large number of Sn particles coarsened in a liquid Pb–Sn eutectic matrix. Our experimental results show that the normalized particle size distribution and the normalized contact distribution are similar to the results for phase-field simulations of grain growth for volume fractions of 52% and 78%, but the kinetics follow the classical diffusion limited particle coarsening prediction.

Simulated microstructures were constructed by randomly placing spherical particles within a simulation volume using the experimentally determined PSDs. An overlap parameter allowed for particle contacts and approximated the observed particle shape distortions. The simulations have a lower mean number of contacts per particle than the experiments. However, when normalized by the mean number of contacts, we find that the contact distribution is approximately independent of the volume fraction for the experimental results, as well as for the simulated microstructures.

By examining the pair correlation functions for both the experiments at 52 vol.% and the simulations, it is found that the particles in the experiment are clustered compared to the random particle simulations. This clustering accounts for most of the difference in the average number of contacts in the experimental and simulated microstructures. We also observe that, when the PSDs are relatively similar, the contact distribution scaled by the average number of contacts is approximately independent of the volume fraction of particles.

At lower volume fractions (<70 vol.%) we find that the number of contacts is proportional to the square of the spherical equivalent particle size in both the experiments and the simulations. However, the experiments and simulations at the higher fraction display a nonlinear relationship between the number of contacts and the square of the particle radius. We attribute this primarily to shape distortions at the higher volume fractions. These experiments show the influence of shape distortions and particle contacts on the coarsening process, and the importance of including shape distortions and particle contacts at high volume fractions in any theory of coarsening.

Acknowledgements

We are grateful for the support of the Physical Sciences Division of NASA and for a NASA Graduate Student Researchers Program fellowship (DJR).

References

[1] Greenwood G. Acta Metall 1956;4:243.
[2] Lifshitz I, Slyozov V. J Phys Chem Solids 1961;19:35.
[3] Wagner C. Z Elektrochem 1961;65:581.
[4] Akaiwa N, Voorhees P. Phys Rev E 1994;49(5):3860.
[5] Voorhees P, Glicksman M. Acta Metall 1984;32(11):2001.
[6] Voorhees P, Glicksman M. Acta Metall 1984;32(11):2013.
[7] Marqusee J, Ross J. J Chem Phys 1984;80(1):536.
[8] Brailsford A, Wynblatt P. Acta Metall 1979;27:489.
[9] Marsh S, Glicksman M. Modelling of coarsening and grain growth. Warrendale, PA: TMS; 1992.
[10] Beenakker C. Phys Rev A 1986;33(6):4482.
[11] Tokuyama M, Kawasaki K. Physica A 1984;123:386.
[12] Marder M. Phys Rev Lett 1985;55(27):2953.
[13] Wang KG, Glicksman ME, Rajan K. Phys Rev 2004;69:061507.
[14] Marsh SP, Glicksman ME. Acta Mater 1996;44(9):3761.
[15] Hardy SC, Voorhees PW. Metall Mater Trans 1988;19A:2713.
[16] Seyhan I, Ratke L, Bender W, Voorhees P. Metall Mater Trans A 1996;27:2470.
[17] Kang C, Yoon D. Metall Mater Trans A 1981;12:65.
[18] Bender W, Ratke L. Acta Metall 1998;46:1125.
[19] Watanabe R, Tada K, Masuda Y. Z Metallkde 1976;67:619.
[20] Mahalingam K, Gu B, Liedl G, Sanders Jr TH. Acta Metall 1987;35(2):483.
[21] Alkemper J, Snyder V, Akaiwa N, Voorhees P. Phys Rev Lett 1999;82(13):2725.

[22] Snyder V, Alkemper J, Voorhees P. Acta Mater 2000;48(10):2689.
[23] Rowenhorst D, Alkemper J, Snyder V, Voorhees P. AIAA conference on international space station utilization, 2001. p. 2001–5092.
[24] Wicksell S. Biometrica 1925;17:84.
[25] Louis P, Gokhale AM. Acta Mater 1996;44:1519.
[26] German RM. Metall Trans A 1987;18:909.
[27] Liu G, Yu H, Qin X. Mater Sci Eng A 2001;326:276.
[28] Wakai F, Enomoto N, Ogawa H. Acta Mater 2000;48:1297.
[29] Gurland J. Trans AIME 1958:452.
[30] Liu P, Lin S. Mater Trans 2002;43:2115.
[31] Liu J, German R. Metall Mater Trans A 2000;31:2607.
[32] Mangan MA, Lauren PD, Shiflet GJ. J Microsc 1997;188:36.
[33] Mendoza R, Alkemper J, Voorhees P. Metall Trans A 2003;34(3):481.
[34] Huang CY, Spanos G, Rosenberg R, Kral M. Acta Mater 2002;50(15):3781.
[35] Alkemper J, Voorhees P. J Microsc-Oxford 2001;201:388.
[36] Krill CE, Deobrich KM, Michels D, Michels A, Rau C, Weitkamp T, et al. In: Ulrich Bonse, editor. Developments in X-ray tomography III, Proc. SPIE, vol. 4503, 2002. p. 205–12.
[37] Tewari A, Gokhale A, German R. Acta Mater 1999;47(13):3721.
[38] Lund A, Voorhees P. Philos Mag 2003;83:1719.
[39] Krill III CE, Chen LQ. Acta Mater 2002;50:3057.
[40] Snyder V, Alkemper J, Voorhees P. Acta Mater 2001;49(4):599.
[41] Digabel H, Lantuájoul C. In: Chermant, JL, editor. Actes du Second Symposium Européen d'Analyse Quantitative des Microstructures en Sciences des Matériaux, Biologie et Médecine, 1978. p. 85–99.
[42] Stoev S. In: Proceedings of 8th international conference on computer graphics, visualization, and interactive digital media, 2000. p. 100–7.
[43] Roerdink JB, Meijster A. FUNDINF: Fundamenta Informatica 2000;41:187.
[44] Fan D, Chen S, Chen L, Chen S, Voorhees P. Acta Mater 2002;50:1895.
[45] Glicksman M, Voorhees P. Metall Trans A 1984;15A:995.
[46] Hillert M. Acta Metall 1965;13:227.
[47] Louat NP. Acta Metall 1974;22:721.
[48] Onoda GY, Liniger EG. Phys Rev Lett 1990;64:2727.
[49] Donev A, Cisse I, Sachs D, Variano E, Stillinger FH, Connelly R, et al. Science 2004;303:990.